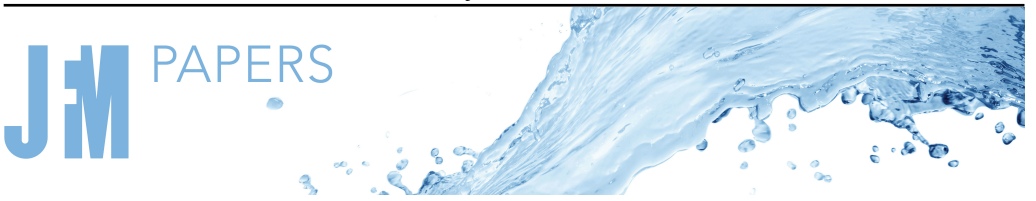
J. Fluid Mech. (2025), *vol.* 1015, A23, doi:10.1017/jfm.2025.10284



How large-scale flow structures affect particle transport in wall turbulence

Jianda Huang[1,†], **Yucheng Jie**[1,†], **Zhiwen Cui**[1,2], **Chunxiao Xu**[1], **Helge I. Andersson**[3] **and Lihao Zhao**[1,4]

[1]AML, Department of Engineering Mechanics, Tsinghua University, Beijing 100084, PR China

[2]College of Mechanical and Vehicle Engineering, Hunan University, Changsha 410082, PR China

[3]Department of Marine Technology, Norwegian University of Science and Technology, Trondheim 7491, Norway

[4]State Key Laboratory of Advanced Space Propulsion, Tsinghua University, Beijing 100084, PR China

Corresponding author: Lihao Zhao, zhaolihao@tsinghua.edu.cn

(Received 31 December 2024; revised 9 May 2025; accepted 19 May 2025)

This study investigates the transport of particles in turbulent channel flow with friction Reynolds number $Re_\tau = 1000$ by direct numerical simulation. We focus on how large-scale flow structures, namely the Qs structures (Lozano-Durán *et al.* 2012, *J. Fluid Mech.*, vol. 694, pp. 100–130), affect the wall-normal transport of particles. Despite occupying less than 10 % of the physical domain, our results highlight the critical role played by Qs structures in the particle transport, namely that the particle number and momentum flux inside the Qs structures are substantially higher than outside. The fraction of particle wall-normal momentum flux inside Qs structures is considerably larger than their volume fraction, suggesting highly efficient transport inside the Qs structures. This prominent role played by Qs structures in the transport of inertial particles is more effective by diminishing the inertia of particles. Notably, the long-distance transport of particles in the wall-normal direction is driven primarily by the continuous effect of Qs structures. In summary, our findings advance the understanding of the effects of Qs structures on particle transport, and demonstrate their significant role in the process.

Key words: particle/fluid flow

1. Introduction

Particle-laden wall-bounded turbulence is ubiquitous in various natural and industrial scenarios. The transport of particles is of great significance for both understanding the

[†]Jianda Huang and Yucheng Jie contributed equally to this work.

© The Author(s), 2025. Published by Cambridge University Press.

https://doi.org/10.1017/jfm.2025.10284 Published online by Cambridge University Press

mechanism of natural phenomena and design of industrial facilities. For instance, transport and dispersion of air pollutants of particulate matters in the atmospheric boundary layer are important environmental problems (Lu *et al.* 2013). In addition, the accumulation and transport of microplastics in water bodies and atmosphere have imposed multiple threats to the sustainability of environments and ecosystems (Xiao *et al.* 2023). Besides, the dynamics of large ore particles during transport in pipelines is significant for the design of hydraulic transport systems in deep-sea mining (Liu *et al.* 2023). Therefore, the understanding of particle transport is essential for addressing environmental concerns and optimising industrial operations. Jianda Huang and Yucheng Jie contributed equally to this work.

Studies on the transport of particles within turbulence have demonstrated its significant relation to flow coherent structures (Fessler, Kulick & Eaton 1994; Marchioli & Soldati 2002; Soldati & Marchioli 2009; Bernardini, Pirozzoli & Orlandi 2013; Bernardini 2014; Berk & Coletti 2020; Wang & Richter 2020; Jie *et al.* 2021, 2022; Motoori, Wong & Goto 2022; Scherer *et al.* 2022). A wide range of coherent structures has been identified in turbulent flows, and their characteristics have been explored extensively (Marusic, Mathis & Hutchins 2010; Haller 2015; Jiménez 2018). These structures are typically multi-scaled and play a crucial role in the momentum transport process. Several techniques are available for detecting coherent structures, with the quadrant analysis (Wallace, Eckelmann & Brodkey 1972; Willmarth & Lu 1972; Lu & Willmarth 1973) classifying points of the flow field based on the quadrant of the parameter plane of streamwise and wall-normal velocity fluctuations. Lozano-Durán *et al.* (2012) generalised the quadrant analysis of the intense Reynolds shear stresses into three-dimensional structures, i.e. Qs structures. They found that Qs structures in turbulent channel flows contribute to 60 % of the total Reynolds shear stress while occupying only less than 10 % of the domain.

The Reynolds number of particle-laden turbulent flows in industrial processes and nature is usually high. Due to limitations in computational capability, previous studies on particle-laden wall-bounded turbulence have largely been restricted to relatively low Reynolds numbers. However, these studies have provided valuable insights into the transport and distribution of particles in wall-bounded turbulence. Due to turbophoresis, particles tend to accumulate in the near-wall regions with low velocity fluctuations (Caporaloni *et al.* 1975; Reeks 1983). Inertial particles have been observed to form particle streaks in the streamwise direction near the wall (Eaton & Fessler 1994). It is revealed that the transport of particles is dominated by sweeps and ejections in the near-wall regions, with sweeps induced by quasi-streamwise vortices transporting particles towards the wall, while ejections re-entrain particles into the buffer layer (Marchioli & Soldati 2002; Picano, Sardina & Casciola 2009; Soldati & Marchioli 2009). Sardina *et al.* (2011, 2012) found that particles tend accumulate into streaks elongated in the streamwise direction, with streamwise length longer than that of velocity streaks. These findings have significantly enhanced our understanding of particle-laden wall turbulence.

Recently, the influence of large-scale flow structures on particle behaviour has garnered growing interest. Large-scale flow structures are more outstanding in turbulent Couette flows than in turbulent channel flows at a similar Reynolds number. Bernardini *et al.* (2013) revealed that particles are transported by large-scale vortices in the turbulent Couette flow, and form large-scale streaky clusters with larger streamwise length and spanwise spacing due to the presence of large-scale flow structures. Advancements in computational capabilities have made it possible to simulate particle-laden turbulence at high Reynolds numbers. Bernardini (2014) found that buffer-layer structures contribute to the wall accumulation of particles with relaxation time comparable to the inner time scale even in turbulence with high Reynolds number, while the transport of particles with

https://doi.org/10.1017/jfm.2025.10284 Published online by Cambridge University Press

high inertia is mainly governed by the outer-layer flow structures. Berk & Coletti (2020) also found that large-scale motions might affect particle statistics in high Reynolds number turbulence. Jie, Andersson & Zhao (2021) demonstrated that the boundary of the quiescent core in turbulent channel flow acts as a barrier on the transport of inertial particles. It has been revealed that particles show different responses to turbulent structures of different scales depending on the Stokes number (Wang & Richter 2020; Jie *et al.* 2022; Gao, Samtaney & Richter 2023). Meanwhile, Scherer *et al.* (2022) found that the formation of sediment ridges often appears under large-scale low-speed streaks. Motoori *et al.* (2022) explained the origin of the multi-scale voids and clusters of particles in terms of the local Stokes number defined by the turnover time of multi-scale vortices. Wei, Wang & Zheng (2024) found that particles tend to accumulate below the turbulent/non-turbulent interface due to the centrifugal effect of large-scale vortices in the outer region.

In summary, the behaviour of particles is highly related to the flow structures in turbulence. However, how large-scale coherent flow structures affect the wall-normal transport of particles in wall turbulence is not well understood. As a specific example, dust particles in a sandstorm originate from the ground surface and can be carried to altitudes of several kilometres. This process may be attributed to turbulent coherent structures in the sandstorm. In particular, the transport of particles is found to be related to $Q2$ and $Q4$ events in wall-bounded turbulence (Marchioli & Soldati 2002; Berk & Coletti 2020; Jie *et al.* 2022). Thus it is natural to speculate that the transportation of sand particles to altitudes of several kilometres may be due to the influence of Qs structures. However, the speculation needs to be examined since the detailed process remains unknown, and there is a need to estimate the transport flux and efficiency inside the Qs structures.

Motivated by the questions raised above, we examine the transport of particles inside and outside the Qs structures in the present study. To the best of the authors' knowledge, this is the first attempt to investigate the effects of Qs structures on the particle transport. For this purpose, we conduct direct numerical simulations of particles in a turbulent channel flow with $Re_\tau = 1000$. Our findings suggest that particle transport inside Qs structures is more efficient compared to that outside them, and the continuous influence of Qs structures drives a long-distance particle transport in the wall-normal direction. In the rest of the paper, § 2 shows the simulation details and method for identifying Qs structures, § 3 provides the results and analyses, and conclusions are drawn in § 4.

2. Method

2.1. *Eulerian fluid phase*

An incompressible Newtonian fluid in turbulent channel flow is considered. The governing equations are

$$\frac{\partial u_i}{\partial x_i} = 0, \quad \frac{\partial u_i}{\partial t} + u_j \frac{\partial u_i}{\partial x_j} = -\frac{1}{\rho}\frac{\partial p}{\partial x_i} + \nu \frac{\partial^2 u_i}{\partial x_j\, \partial x_j}, \tag{2.1}$$

where x_i $(i = 1, 2, 3)$ (or x, y, z) denote the streamwise, wall-normal and spanwise directions, respectively. Correspondingly, u_i $(i = 1, 2, 3)$ (or u, v, w) represent the respective flow velocity components. Also, p is the pressure, and ρ and ν are the density and kinematic viscosity of the fluid, respectively. Based on the frictional velocity $u_\tau = \sqrt{\tau_w/\rho}$, where τ_w is the mean wall shear stress, the viscous time scale and the viscous length scale are defined as $\tau_\nu = \nu/u_\tau^2$ and $\delta_\nu = \nu/u_\tau$, respectively. Hereafter, physical variables normalised by the viscous scales are marked with a superscript $+$. The boundary conditions are periodic in the streamwise and spanwise directions, while a no-slip/no-penetration condition is adopted at both walls ($y = 0, 2h$, where h denotes

https://doi.org/10.1017/jfm.2025.10284 Published online by Cambridge University Press

Case	Re_τ	Domain size	Grids	Δy_w^+	Δy_c^+	N_p per sort	St_ν range
L1k	1000	$8\pi h \times 2h \times 3\pi h$	$2304 \times 384 \times 1728$	0.8689	7.6545	5×10^5	0−200

Table 1. Simulation parameters of the particle-laden turbulent channel flow, where Δy_w^+ and Δy_c^+ represent the grid spacings at the wall and the centreline, respectively, and N_p is the particle number of each type.

the half-height of the channel). To solve (2.1), a pseudo-spectral method is employed in the streamwise and spanwise directions, while a second-order finite difference scheme is adopted in the wall-normal direction. A second-order Adams–Bashforth scheme is used in time evolution (Zhao & Andersson 2012; Jie *et al.* 2022).

2.2. *Lagrangian particle phase*

The particles suspended in the fluid are assumed to be spherical, with density ρ_p much larger than the fluid density, diameter $D_p = 2a$ smaller than the Kolmogorov length scale η, and response time $\tau_p = 2a^2\rho_p/9\rho\nu$. We consider dilute conditions where the volume fraction of particles is sufficiently low that particle interactions and feedback from the particles on the fluid are neglected. Gravity is neglected for the sake of highlighting the effects of particle inertia and turbulent structures. The particle Froude numbers $Fr_p = U_b/(g\tau_p)$ considered in the present study are all larger than 100, where U_b is the bulk velocity of the channel flow, supporting that the gravity effect is negligible compared with the effect of the bulk motion of fluid flow (Milici *et al.* 2014). One should note that the gravity effect in the wall-normal direction might be non-negligible compared to the turbophoresis effect, even when the settling number is smaller than 1 (Bragg, Richter & Wang 2021). All the particles considered in the present study have normalised diameter $D_p^+ = 0.6 < 1$, which leads the magnitude of the Saffman lift force to be much smaller than the Stokes drag force (Costa, Brandt & Picano 2020). Therefore, we neglect the lift force in the present study, while one should note that the effect of the wall-normal lift force may arise for the particles embedded in the sublayer, where these particles normally stay for a long time. The density of the particle is sufficiently larger than that of fluid, so only the Stokes drag with a semi-empirical correction is considered (Schiller & Naumann 1933), while the average particle Reynolds numbers $Re_p = 2a\,\|\boldsymbol{u} - \boldsymbol{v}\|/\nu$ are smaller than 1 in the present study (not shown). Therefore, the governing equations of the particles are

$$\frac{\mathrm{d}x_{p,i}}{\mathrm{d}t} = u_{p,i}, \quad \frac{\mathrm{d}u_{p,i}}{\mathrm{d}t} = \frac{1}{\tau_p}(u_{f@p,i} - u_{p,i})\left(1 + 0.15\,Re_p^{0.687}\right), \tag{2.2}$$

where $x_{p,i}$ is the location of the particle, and $u_{p,i}$ is the velocity of the particle, while $u_{f@p,i}$ is the local fluid velocity at the particle location obtained by a second-order Lagrangian interpolation (Zhao & Andersson 2012; Jie *et al.* 2022). The Stokes number of a particle is defined as $St_\nu = \tau_p/\tau_\nu$. Periodic boundary conditions are imposed in both the streamwise and spanwise directions for particles. The collision between the particles and the walls is fully elastic. An explicit second-order Adams–Bashforth scheme is employed to solve (2.2) (Zhao & Andersson 2012; Jie *et al.* 2022). The simulation parameters are provided in table 1. Particles are released randomly in the domain after the turbulent channel flow is fully developed ($t^+ = 0$).

2.3. *Voronoï tessellation*

The Voronoï tessellation is employed to quantify the preferential accumulation of particles both inside and outside the Qs structures (Monchaux, Bourgoin & Cartellier 2010;

https://doi.org/10.1017/jfm.2025.10284 Published online by Cambridge University Press

Nilsen, Andersson & Zhao 2013; Baker *et al.* 2017; Yuan *et al.* 2018). The location of a particle is treated as the centre of the corresponding Voronoï cell. The cell contains all the volumes that are closer to its centre rather than to the centres of other cells. The Voronoï tessellation is unique for a given particle field. The volume V of the Voronoï cell can reflect the local concentration of particles. Specifically, the inverse of the Voronoï volume V represents the local concentration, i.e. $c_{loc} = 1/V$. In addition, the history of local accumulation experienced by a particle can be tracked by monitoring the Voronoï volume along its trajectory.

2.4. *Identification of Qs structures*

To quantify the effects of Qs structures on the transport of particles, the method proposed by Lozano-Durán *et al.* (2012) is adopted to identify the Qs structures. The Qs structures are defined as connected regions satisfying the threshold

$$|\tau(\boldsymbol{x})| > H\, u'_{rms}(y)\, v'_{rms}(y), \tag{2.3}$$

where $\tau(\boldsymbol{x}) = -u'(\boldsymbol{x})\, v'(\boldsymbol{x})$ is the instantaneous contribution to Reynolds shear stress at the location $\boldsymbol{x}$, and the parameter $H = 1.75$ is determined through a percolation analysis. The bold $\boldsymbol{x}$ represents a spatial point with three components, $\boldsymbol{x} = (x, y, z)$. Also, $u'_{rms}(y)$ and $v'_{rms}(y)$ are the root mean square of the streamwise and wall-normal velocity fluctuations, respectively, which are functions of the wall-normal coordinate y alone because they are averaged over homogeneous streamwise and spanwise directions. In brief, the percolation analysis calculates the ratio of the volume of the largest identified Qs to the total volume satisfying (2.3) and total number of identified Qs structures normalised by its maximum over H, with the threshold $H = 1.75$ chosen to maximise the number of identified Qs structures. Initially, regions that satisfy (2.3) are identified. These regions are then classified into different clusters based on the connectivity of points. The resulting clusters represent structures of instantaneous pointwise Reynolds shear stress, referred to as Qs structures. The Qs structures are grouped into different sets according to the quadrant of the mean velocity fluctuations (u'_m, v'_m) in the domain Ω of the cluster, which are defined as

$$u'_m = \frac{\int_\Omega u'\,\mathrm{d}V}{\int_\Omega \mathrm{d}V}, \quad v'_m = \frac{\int_\Omega v'\,\mathrm{d}V}{\int_\Omega \mathrm{d}V}. \tag{2.4}$$

Note that the sign of v' in the upper half-channel $h < y < 2h$ is inverted to identify the Qs structures correctly. More specifically, Qs refers to quadrant (Q) events, which include $Q1$ events with $u'_m > 0$ and $v'_m > 0$, $Q2$ events with $u'_m < 0$ and $v'_m > 0$, $Q3$ events with $u'_m < 0$ and $v'_m < 0$, and $Q4$ events with $u'_m > 0$ and $v'_m < 0$. The $Q1$ and $Q3$ structures are collectively defined as the Q^+ structures, while the $Q2$ and $Q4$ structures are classified as Q^- structures. Additionally, $\phi(X)$ denotes the fraction of a physical variable X in the area domain of Qs structures at different wall-normal locations:

$$\phi(X)_{Qi} = \frac{\Sigma_{Qi(\Phi)} X}{\Sigma_\Phi X}, \tag{2.5}$$

where Φ represents the two-dimensional area domain of all Qs structures intersecting a specific wall-normal plane at y^+ , and $Qi(\Phi)$ stands for the area domain of Qi structures in the area domain Φ, where i can take the values 1, 2, 3 or 4.

https://doi.org/10.1017/jfm.2025.10284 Published online by Cambridge University Press

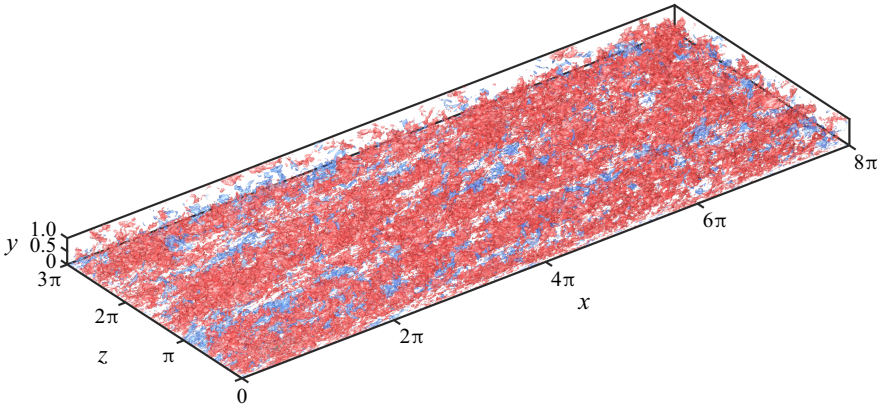


Figure 1. Instantaneous Qs structures in the lower half of the turbulent channel flow at $Re_\tau = 1000$. The red clusters are $Q2$ structures, while the blue clusters are $Q4$ structures.

Case	N_1	N_2	N_3	N_4	V_1	V_2	V_3	V_4	ΣV_i
L1k	0.18	0.35	0.18	0.29	0.003	0.074	0.002	0.014	0.093
L950	0.18	0.33	0.19	0.31	0.004	0.056	0.006	0.025	0.091

Table 2. The number fraction N_i and the volume fraction V_i of different Qs structures. The data of L950 from Lozano-Durán *et al.* (2012) in turbulent channel flow at $Re_\tau = 950$ are included for comparison.

3. Results

3.1. *Statistics of Qs structures*

Figure 1 shows the instantaneous distribution of $Q2$ and $Q4$ structures in the channel flow. The $Q2$ structures occupy a larger proportion of the domain compared to the $Q4$ structures. Table 2 presents the number fraction N_i and volume fraction V_i of various Qs structures. The statistics metrics for both N_i and V_i from the present L1k case are in a good agreement with the results of Lozano-Durán *et al.* (2012). It is evident that the majority of Qs structures are $Q2$ structures, followed by $Q4$ structures. All Qs structures collectively occupy only approximately 10 % of the entire domain, as indicated in table 2, consistent with Lozano-Durán *et al.* (2012).

Figure 2(a) displays the fraction of the total Reynolds shear stress carried by the Q^- structures. The present results closely match the statistics reported by Lozano-Durán *et al.* (2012). These fractions vary with changes in the wall-normal distance. The $Q4$ structures exhibit a lower fraction of the total Reynolds stress compared to $Q2$ structures. The Q^- structures can be further classified into attached and detached types, depending on whether they are in contact with the wall. Consistent with Lozano-Durán *et al.* (2012), the attached Q^- structures account for approximately 60 % of the total Reynolds shear stresses. Specifically, the sum of the fractions for the attached $Q2$ and $Q4$ structures is approximately 60 % in the near-wall region, and even exceeds 60 % away from the wall. Figure 2(b) shows the volume fractions of different Qs structures at various wall-normal locations. The volume fraction of all Qs structures at different wall-normal locations, denoted as $\phi(V)_{Qs}$, ranges from approximately 0.08 to 0.10, consistent with the results in table 2. This also suggests that $Q1$ and $Q3$ structures, i.e. the Q^+ structures, occupy a relatively small volume fraction, while Q^- structures dominate. Among the Q^- structures, the volume fraction of the $Q2$ structures is larger than that of the $Q4$ structures.

https://doi.org/10.1017/jfm.2025.10284 Published online by Cambridge University Press

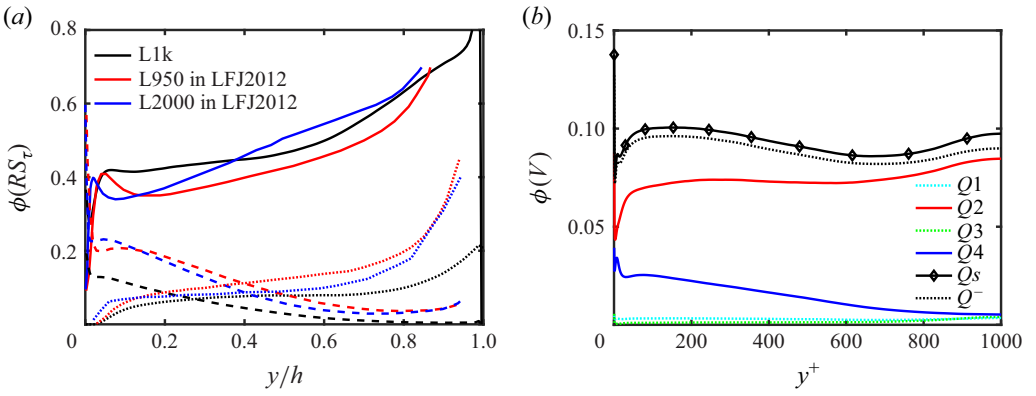


Figure 2. (*a*) Fraction of the total Reynolds stresses from: attached $Q2$ (solid lines), attached $Q4$ (dashed lines), and detached Q^- (dotted lines). Black lines stand for the present case L1k, and red and blue lines represent case L950 ($Re_\tau \approx 950$) and case L2000 ($Re_\tau \approx 2000$) in Lozano-Durán *et al.* (2012) (referred to as LFJ2012), respectively. (*b*) Volume fraction of all Qs structures versus the wall-normal location y^+.

Lozano-Durán *et al.* (2012) demonstrated that attached Q^- structures are responsible for approximately 60 % of the total Reynolds shear stress, despite covering less than 8 % of the total volume at every wall-normal height. This underscores the important role of Q^- structures in momentum transport in wall-bounded turbulence. In addition, the wall-normal transport and the multi-scale clusters of particles near the walls are both related to the sweeps and ejections in wall-bounded turbulence (Marchioli & Soldati 2002; Berk & Coletti 2020; Jie *et al.* 2022). In the subsequent subsections, we proceed to investigate the distribution of particles both inside and outside the Qs structures, as well as the effects of these Qs structures on the wall-normal transport of particles.

3.2. *Distribution of particles inside and outside Qs structures*

The Voronoï tessellation is used to quantify the distribution of particles both inside and outside Qs structures. Figure 3 shows the Voronoï volume of particles inside and outside the Qs structures versus the wall-normal position y^+. Note that the inverse of the Voronoï volume serves as an indicator of the local concentration of particles. The small difference between the black triangles and black circles indicates that the particle concentration outside the Qs structures is approximately equal to the overall particle concentration in the domain. This is expected because the region outside the Qs structures occupies approximately 90 % of the entire domain. The concentration of particles with $St_v = 0$ inside the Qs structures is similar to that outside the Qs structures due to the tracer behaviour of particles with no inertia. However, the concentrations of particles inside and outside the Qs structures become increasingly different as particle inertia increases. For instance, for particles with $St_v = 30$, the mean Voronoï volume of particles inside $Q2$ structures is greater than that in $Q4$ structures when $y^+ > 100$, indicating that particle concentration in $Q2$ structures is lower than that in $Q4$ structures. In the central region of the channel, the particle concentration outside the Qs structures is higher than that inside either the $Q2$ or $Q4$ structures. The identification of the Qs structures reveals that they correspond to regions with relatively intense fluctuations. Therefore, the phenomenon that particles tend to accumulate outside Qs structures suggests that particles tend to accumulate in low turbulence intensity regions. This phenomenon may reflect another aspect of the turbophoresis mechanism, where particles tend to migrate towards and accumulate near the wall. The near-wall region is typically characterised by low turbulence intensity, and within such environments, particles possess relatively low

https://doi.org/10.1017/jfm.2025.10284 Published online by Cambridge University Press

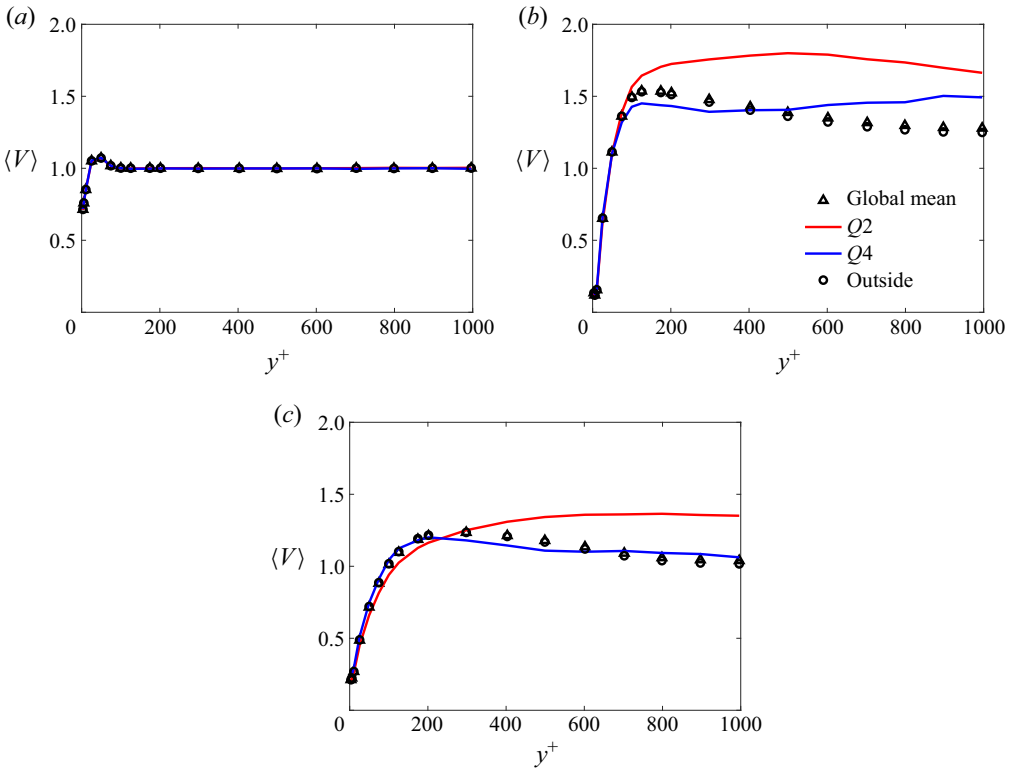


Figure 3. Mean Voronoï volumes of particles with (*a*) $St_v = 0$, (*b*) $St_v = 30$ and (*c*) $St_v = 200$ inside and outside Qs structures versus the wall-normal height y^+.

kinetic energy, making it more difficult for them to escape. As a result, particles exhibit prolonged residence times in these regions. This observation aligns with the findings of Liu *et al.* (2020), who reported that particle clusters tend to persist in areas of low enstrophy and strain rate throughout their lifetimes. Such low-turbulence zones provide favourable conditions for the stability and survival of particle clusters, due to the lack of strong turbulent fluctuations to break them apart or eject them.

Furthermore, figure 4 shows the particle number fractions $\phi(N_p)$ inside the Qs structures versus the wall-normal location. The tracer particles perfectly follow the local fluid elements, resulting in their random distribution throughout the entire domain. Therefore, the number fractions of tracer particles inside the Qs structures are equivalent to the volume fraction of the corresponding Qs structures, as displayed in figure 2. As particle inertia increases, the number fractions of particles inside the Qs structures remain comparable to the volume fractions of the Qs structures in the near-wall regions. However, in the central region of the channel, the number fraction of particles inside Qs structures is smaller than the volume fraction of Qs structures. This indicates that particles with higher inertia do not tend to accumulate inside Qs structures but instead avoid regions of intense fluctuations such as the Qs structures. This is in line once again with the turbophoresis mechanism.

3.3. *Wall-normal transport of particles inside Qs structures*

To study the wall-normal transport of particles, the wall-normal flux and transport efficiency of particles inside and outside Qs structures are examined. The particle number

https://doi.org/10.1017/jfm.2025.10284 Published online by Cambridge University Press

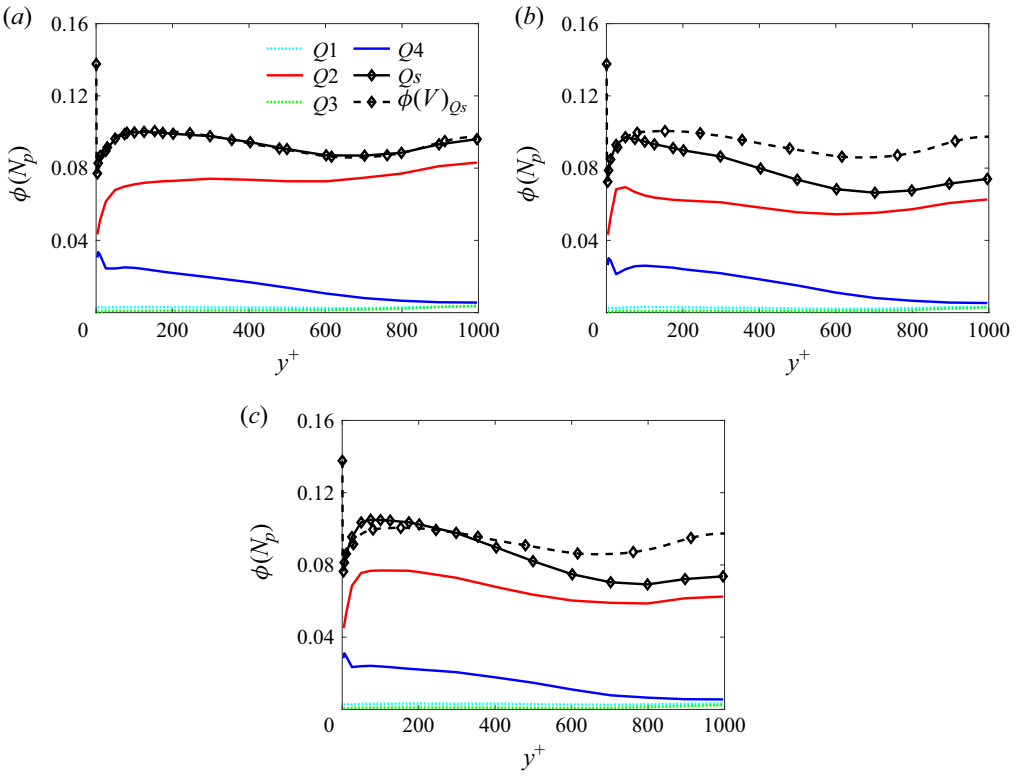


Figure 4. Number fractions of particles with (*a*) $St_v = 0$, (*b*) $St_v = 30$ and (*c*) $St_v = 200$ inside Qs structures versus the wall-normal height y^+.

flux ($\mathcal{F}_N$) and momentum flux ($\mathcal{F}_M$) in the wall-normal direction through a small wall-parallel plane with area dS during a short period dt are considered. We begin by considering these expressions from an Eulerian perspective. For a given particle type, the density distribution is denoted by $\rho(x, y, z)$, and the concentration distribution is defined as $c(x, y, z) = \rho(x, y, z)/m_p$, where m_p is the mass of a single particle. The wall-normal velocity distribution of particles is given by $v_y(x, y, z)$. Over a short time interval dt, the total mass of particles of a specific type crossing a wall-parallel plane with area dS (at a fixed $y = \text{const}$) is

$$\mathrm{d}M = \rho(x, y, z)\, v_y(x, y, z)\, \mathrm{d}t\, \mathrm{d}S = m_p\, c(x, y, z)\, v_y(x, y, z)\, \mathrm{d}t\, \mathrm{d}S. \tag{3.1}$$

Thus the number of particles crossing the reference plane is

$$\mathrm{d}N_p = \frac{\mathrm{d}M}{m_p} = c(x, y, z)\, v_y(x, y, z)\, \mathrm{d}t\, \mathrm{d}S. \tag{3.2}$$

Averaging over the x and z directions, the wall-normal particle number flux becomes

$$\mathcal{F}_N(y) = \left\langle \frac{\mathrm{d}N_p}{\mathrm{d}t\, \mathrm{d}S} \right\rangle_{x,z} = \langle c(x, y, z)\, v_y(x, y, z) \rangle_{x,z}, \tag{3.3}$$

where $\langle\cdot\rangle_{x,z}$ denotes averaging in the x and z directions. Since our simulation uses a Lagrangian point particle method, the local concentration $c(x, y, z)$ must be evaluated in a Lagrangian manner. As described in § 2.3, the local concentration at the particle position

https://doi.org/10.1017/jfm.2025.10284 Published online by Cambridge University Press

(x_p, y_p, z_p) is given by the inverse of the Voronoï volume, namely, $c(x_p, y_p, z_p) = c_{loc} = 1/V(x_p, y_p, z_p)$. Hence the averaged wall-normal particle number flux can be written as

$$\begin{aligned}\mathcal{F}_N(y) &= \langle c(x, y, z)\, v_y(x, y, z)\rangle_{x,z} \\ &= \frac{1}{N_{tot}} \sum_{y-\Delta/2<y_p<y+\Delta/2} v_{y,p}(x_p, y_p, z_p)\, c(x_p, y_p, z_p) \\ &= \frac{1}{N_{tot}} \sum_{y-\Delta/2<y_p<y+\Delta/2} \frac{v_{y,p}(x_p, y_p, z_p)}{V(x_p, y_p, z_p)} \\ &= \frac{1}{N_{tot}} \sum_{y-\Delta/2<y_p<y+\Delta/2} \mathcal{F}_N^p,\end{aligned} \tag{3.4}$$

where N_{tot} is the total number of particles within the wall-normal slab $y_p \in [y - \Delta/2, y + \Delta/2]$, Δ is the slab thickness, $v_{y,p}$ is the instantaneous wall-normal velocity of particle at its current location, and the instantaneous particle flux associated with a single particle is defined as

$$\mathcal{F}_N^p = \frac{v_{y,p}(x_p, y_p, z_p)}{V(x_p, y_p, z_p)}. \tag{3.5}$$

Similarly, the total wall-normal momentum carried by particles across a wall-parallel plane with area $\mathrm{d}S$ is

$$\rho(x, y, z)\, v_y(x, y, z)\, \mathrm{d}t\, \mathrm{d}S \times v_y(x, y, z) = m_p\, c(x, y, z)\, v_y^2(x, y, z)\, \mathrm{d}t\, \mathrm{d}S. \tag{3.6}$$

Therefore, the averaged wall-normal momentum flux of particles is

$$\begin{aligned}\mathcal{F}_M(y) &= \left\langle \frac{m_p c(x, y, z)\, v_y^2(x, y, z)\, \mathrm{d}t\, \mathrm{d}S}{\mathrm{d}t\, \mathrm{d}S} \right\rangle_{x,z} \\ &= \langle m_p c(x, y, z)\, v_y^2(x, y, z)\rangle_{x,z} \\ &= \frac{m_P}{N_{tot}} \sum_{y-\Delta/2<y_p<y+\Delta/2} v_{y,p}^2(x_p, y_p, z_p) c(x_p, y_p, z_p) \\ &= \frac{m_p}{N_{tot}} \sum_{y-\Delta/2<y_p<y+\Delta/2} \frac{v_{y,p}^2(x_p, y_p, z_p)}{V(x_p, y_p, z_p)} \\ &= \frac{m_p}{N_{tot}} \sum_{y-\Delta/2<y_p<y+\Delta/2} \mathcal{F}_M^p,\end{aligned} \tag{3.7}$$

with the instantaneous wall-normal momentum flux $\mathcal{F}_M^p$ carried by each particle defined as

$$\mathcal{F}_M^p = \frac{v_{y,p}^2(x_p, y_p, z_p)}{V(x_p, y_p, z_p)}. \tag{3.8}$$

For brevity, the particle mass m_p, constant for a specific particle type, is omitted in the subsequent discussions of wall-normal momentum flux:

$$\mathcal{F}_M(y) = \frac{1}{N_{tot}} \sum_{y-\Delta/2<y_p<y+\Delta/2} \frac{v_{y,p}^2(x_p, y_p, z_p)}{V(x_p, y_p, z_p)}. \tag{3.9}$$

https://doi.org/10.1017/jfm.2025.10284 Published online by Cambridge University Press

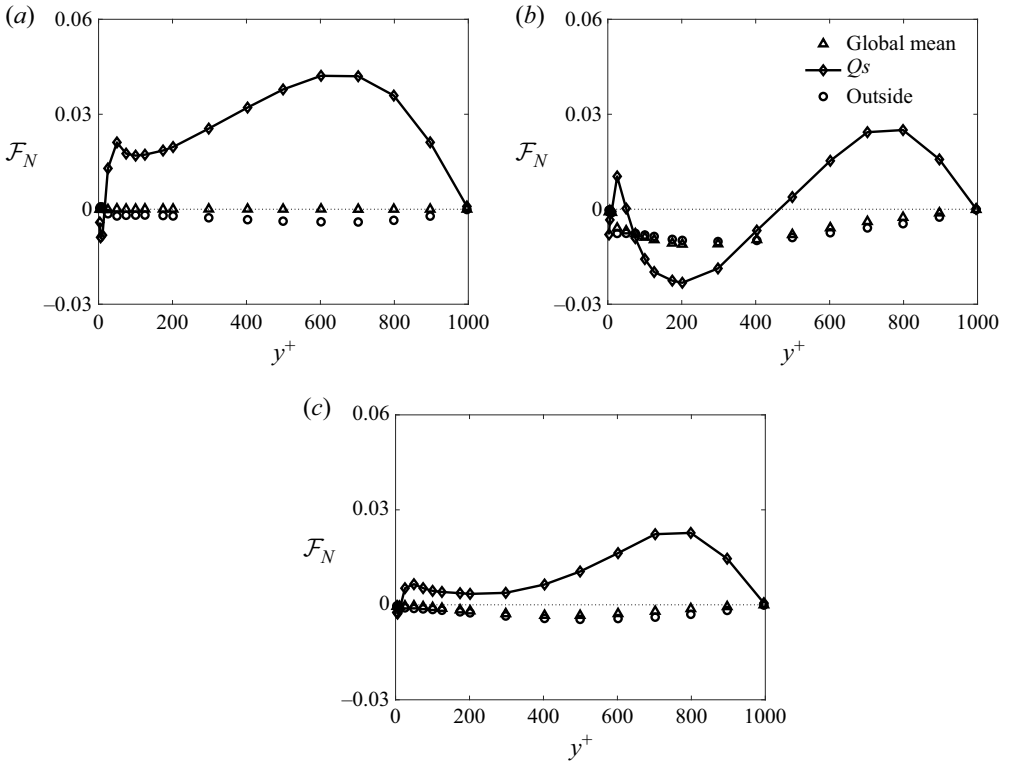


Figure 5. The average particle number flux $\mathcal{F}_N$ at different wall-normal locations y^+ for particles with (*a*) $St_v = 0$, (*b*) $St_v = 30$ and (*c*) $St_v = 200$.

As the analysis focuses solely on the fractions of wall-normal momentum flux across different St_v, this choice does not affect the comparison of statistics for particles of the same type. Likewise, the streamwise momentum flux can be expressed in a similar manner:

$$\mathcal{F}_M^x(y) = \frac{1}{N_{tot}} \sum_{y-\Delta/2<y_p<y+\Delta/2} \frac{v_{x,p}^2(x_p, y_p, z_p)}{V(x_p, y_p, z_p)}, \tag{3.10}$$

where $v_{x,p}$ is the instantaneous streamwise velocity of particle at its current location.

Note that the total flux through Qs structures depends on the number of particles inside them. In contrast, the fluxes $\mathcal{F}_N$ and $\mathcal{F}_M$ capture the contribution per particle. This per-particle perspective isolates the intrinsic efficiency of Qs structures in enhancing transport, regardless of the overall number of particles contained inside these structures. Our analysis thus focuses on the local, per-particle transport effects, highlighting that even though fewer particles reside inside the Qs regions, each particle in these structures experiences a markedly enhanced transport effect compared to those outside.

3.3.1. *Wall-normal flux*

The particle number flux versus the wall-normal position for particles with $St_v = 0, 30, 200$ is shown in figure 5. A positive value represents the flux of particles towards the channel centre, while a negative value denotes flux towards the walls. The particle number flux inside the Qs structures significantly surpasses that outside them,

https://doi.org/10.1017/jfm.2025.10284 Published online by Cambridge University Press

particularly prominent for $St_v = 0$ and 200 particles (figure 5*a*,*c*). The ratio between the flux inside and outside Qs structures can even approach approximately 10 at some y^+ locations. This indicates that the particle number flux inside the Qs structures is high, raising the possibility of more efficient particle transport inside the Qs structures than that outside them. Interestingly, Bo (2021) investigated dust transport during a cold-front-induced dust storm, and found that large-scale ejection and sweep events play a dominant role in the vertical transport of dust particles. While the structures identified by Bo (2021) are not defined in the same way as the Qs structures used in the present study, they encompass similar energetic regions of the flow. As such, these field observations offer strong qualitative support for our conclusion that Qs structures serve as highly efficient pathways for particle transport in wall-bounded turbulence.

The negative values for black circles in figure 5 indicate that, on average, particles outside the Qs structures are consistently migrating towards the wall. For $St_v = 0$ and 200 particles, the number flux inside the Qs structures remains always positive, indicating a consistent migration of particles towards the channel centre. This behaviour is likely influenced by the presence of $Q2$ structures, which constitute the largest volume fraction among the Qs structures. However, the sign of the number flux of $St_v = 30$ particles varies with wall-normal position. The wall-normal distributions of $St_v = 30$ and 200 particles have not yet reached a completely statistically steady state. In turbulent channel flows, it takes a long time for the wall-normal distribution of particles to reach a statistically steady state (Sardina *et al.* 2012; Bernardini 2014). The present simulation spans approximately 4000 temporal wall units. However, the primary objective of this study is to examine the instantaneous processes of particle transport and their modulation by Qs structures. Our focus is on how individual particles interact with Qs structures, and how these interactions influence their transport. Such interactions occur over relatively short time scales compared to the lifetime of Qs structures (Lozano-Durán & Jiménez 2014; Jie *et al.* 2022), therefore meaningful insights can be obtained without relying on statistically converged particle concentration fields. As a result, although a net flux of particles towards the wall is observed, as indicated by the negative global mean values in figures 5(*b*) and 5(*c*), the qualitative conclusions of this study remain valid. This approach is consistent with our previous work (Jie *et al.* 2022), which investigated the formation of near-wall particle streaks and the interaction between inertial particles with a certain Stokes number and the primary Qs structures, to which these particles respond most quickly and efficiently and thus form near-wall streaky patterns in a short time.

Furthermore, the particle momentum flux is examined in the presence of the Qs structures. In figure 6, an instantaneous field shows both the momentum flux of particles in the wall-normal direction and the geometry of the $Q2$ and $Q4$ structures. Note that the sizes of spheres in figure 6 represent the values of the instantaneous wall-normal momentum flux $\mathcal{F}_M^p$ of particles. Several large-size spheres are clearly discernible inside and around the $Q2$ and $Q4$ structures, indicating a large wall-normal particle momentum flux of $St_v = 30$ particles inside and around the Q^- structures. Conversely, spheres are rarely observed in the region beyond the Q^- structures. The spheres outside the Q^- structures are smaller compared to those inside the Q^- structures, suggesting a reduced wall-normal particle momentum flux in the absence of the Q^- structures.

To quantitatively analyse the impact of Qs structures on the wall-normal momentum flux, figure 7 shows the mean momentum flux $\mathcal{F}_M$ of particles versus the wall-normal location y^+. It is evident that the particle momentum flux inside the Qs structures is approximately 2–3 times greater than the momentum flux outside them. Figure 7(*a*) shows the momentum flux of tracer particles, with the particle momentum flux inside

https://doi.org/10.1017/jfm.2025.10284 Published online by Cambridge University Press

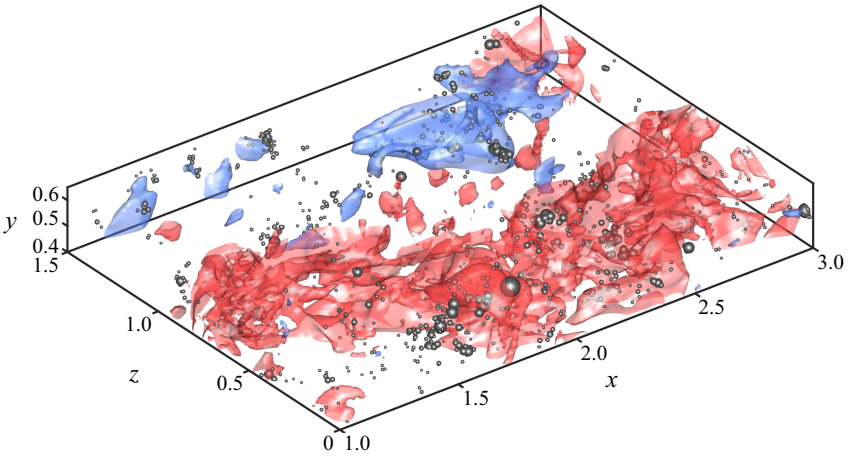


Figure 6. The instantaneous distribution of the momentum flux of particles with $St_v = 30$ with the presence of the Qs structures. The $Q2$ structures are highlighted in red, while $Q4$ structures are in blue. Black spheres represent the particles with their sizes indicating the values of the instantaneous wall-normal momentum flux $\mathcal{F}_M^p$ of particles. Note that the black spheres are drawn only when the instantaneous particle momentum flux exceeds the mean value of particle momentum flux in the domain.

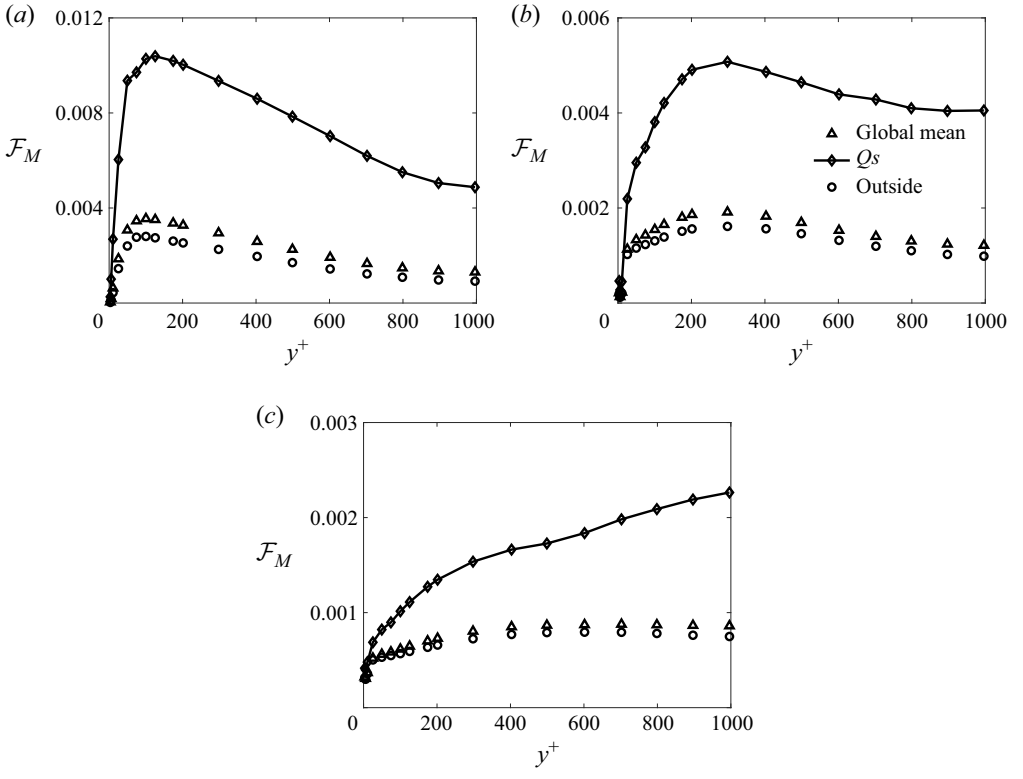


Figure 7. The mean wall-normal particle momentum flux $\mathcal{F}_M$ inside and outside Qs structures versus the wall-normal position y^+: (*a*) $St_v = 0$, (*b*) $St_v = 30$, and (*c*) $St_v = 200$.

https://doi.org/10.1017/jfm.2025.10284 Published online by Cambridge University Press

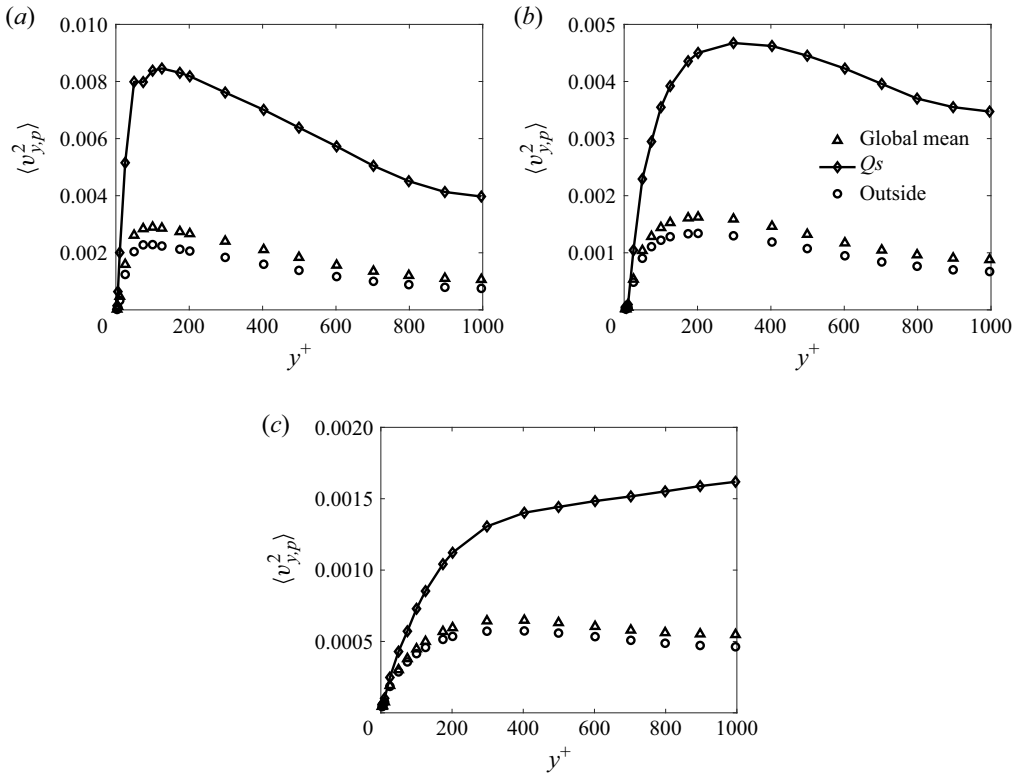


Figure 8. The mean squared wall-normal particle velocity profile inside and outside Qs structures versus the wall-normal position y^+: (*a*) $St_v = 0$, (*b*) $St_v = 30$, and (*c*) $St_v = 200$.

the Qs structures peaking in the buffer layer around $y^+ \approx 100$. However, the peak location varies, ranging from $y^+ \approx 300$ for $St_v = 30$ particles to $y^+ \approx 1000$ for $St_v = 200$ particles, suggesting the possible presence of a multi-scale effect. From Eq. (3.7), the particle momentum flux is determined by the squared wall-normal velocity of particles and the inverse of the Voronoï volume. As shown in figure 8, the distribution of the squared wall-normal velocity of particles closely resembles that of the particle momentum flux. In contrast, the distribution of the Voronoï volume does not change significantly across the wall-normal direction (figure 3). This indicates that the particle momentum flux profile is predominantly governed by the wall-normal velocity distribution of the particles. By examining figure 8, we observe that tracer particles, which faithfully follow the fluid, reproduce the wall-normal velocity profile of the fluid itself. As particle inertia increases, their ability to respond to fluid motion diminishes. This inertial filtering effect causes the peak of the wall-normal velocity distribution to shift outwards, eventually approaching the channel centre. This trend strongly suggests that particles with different Stokes numbers interact preferentially with Qs structures of different characteristic scales. This can be supported by the observation that there is a strong correlation between the particle fluxes and fluid momentum fluxes where particles with small inertia are transferred by coherent sweep and ejection events in the buffer layer (Marchioli & Soldati 2002), while particles with larger Stokes numbers are transferred by large-scale Qs structures in the log layer (Jie *et al.* 2022). Therefore, a plausible explanation is that with increasing inertia, particles tend to interact more effectively with larger-scale Qs structures, which are typically found

https://doi.org/10.1017/jfm.2025.10284 Published online by Cambridge University Press

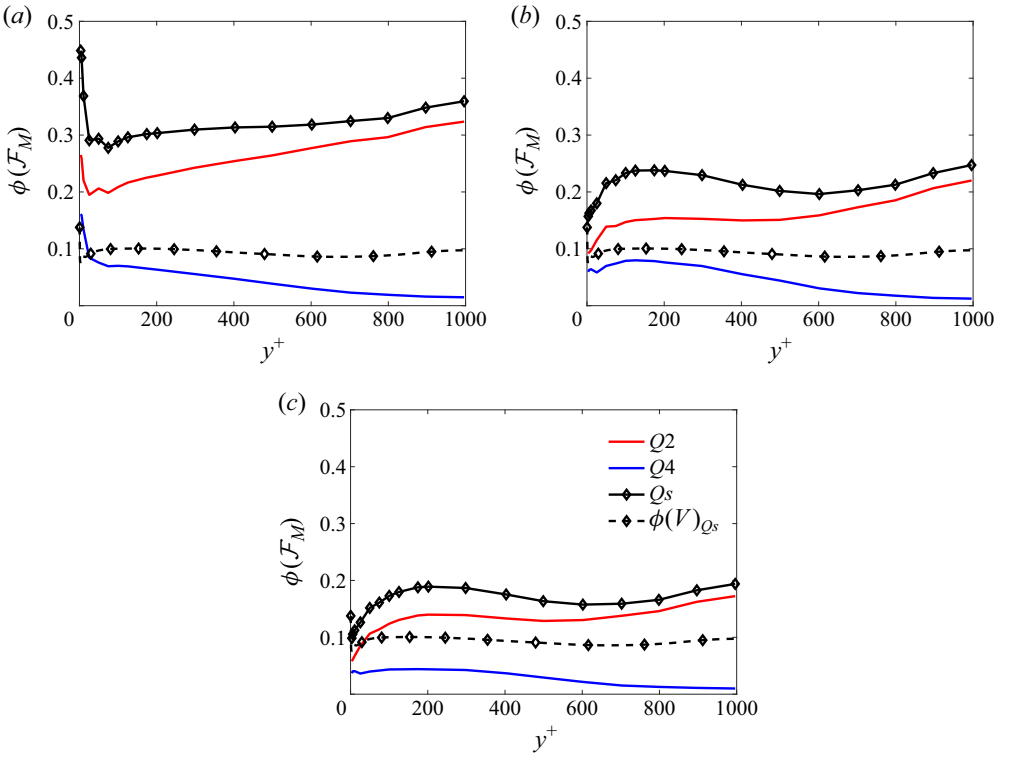


Figure 9. Fractions of wall-normal particle momentum flux inside different Qs structures for particles with (*a*) $St_v = 0$, (*b*) $St_v = 30$ and (*c*) $St_v = 200$ at different positions. The dashed lines with diamonds represent the volume fractions of the Qs structures.

farther from the wall. This interaction underlies the observed outward shift in the peak of the particle momentum flux profile.

3.3.2. *Efficiency of wall-normal transport*

The efficiency of the wall-normal transport of particles inside and outside the Qs structures is assessed by comparing the fractions of flux inside and outside the Qs structures. Figure 9 shows the fractions of wall-normal momentum fluxes of particles with $St_v = 0$–200 at different locations. For tracers in figure 9(*a*), the momentum flux inside the Qs structures accounts for approximately 30 % of the total momentum flux. However, the Qs structures themselves occupy less than 10 % of the domain volume. Hence less than 10 % of the domain is responsible for transporting 30 % of the total wall-normal momentum flux, implying an extremely efficient transport by the Qs structures. This efficiency extends to inertial particles as well. For $St_v = 30$ particles, the fraction inside the Qs structures approximates 20–25 % in the outer layer, while for $St_v = 200$ particles, it can reach 15–20 % in the outer layer. Among the three types of particles, tracer particles exhibit the most efficient transport of wall-normal momentum flux by the Qs structures. With higher particle inertia, this efficiency gradually decreases. However, even for $St_v = 200$, the fraction of flux inside the Qs structures remains approximately twice as large as the volume fraction of the Qs structures. Moreover, the $Q2$ structures play a more important role in the transport of momentum flux compared to the $Q4$ structures. This is attributed to the higher volume fraction of $Q2$ structures, as shown in figure 2(*b*).

https://doi.org/10.1017/jfm.2025.10284 Published online by Cambridge University Press

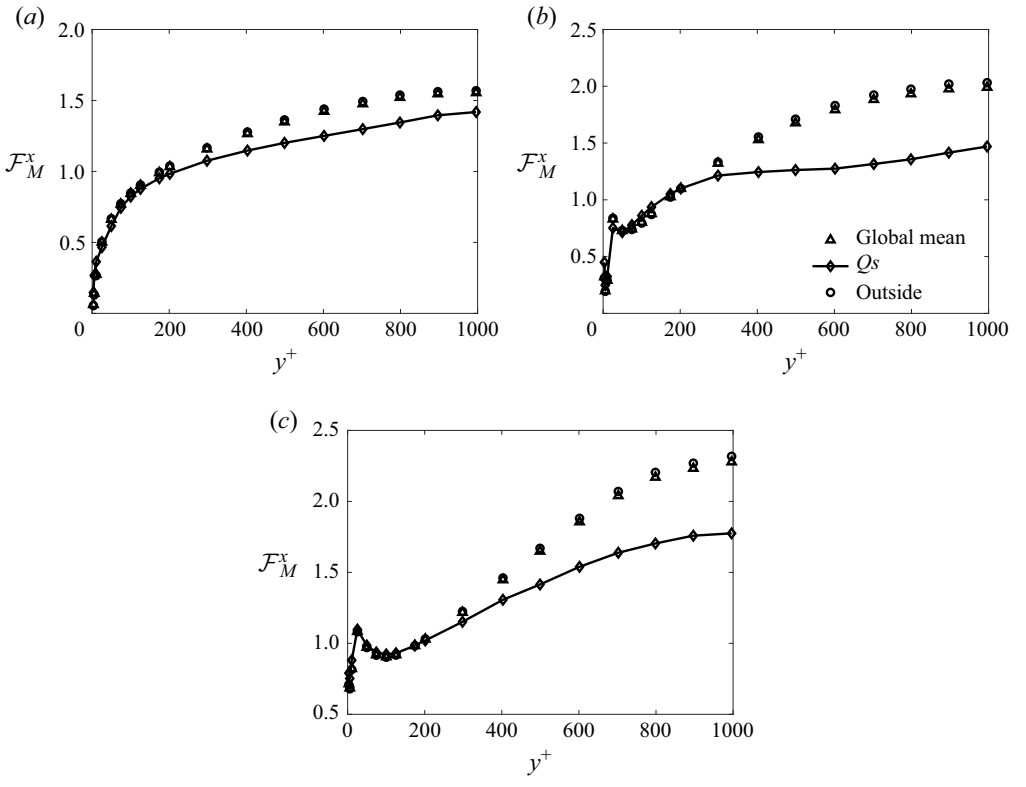


Figure 10. The mean streamwise particle momentum flux $\mathcal{F}_M^x$ inside and outside Qs structures versus the wall-normal position y^+: (*a*) $St_v = 0$, (*b*) $St_v = 30$, and (*c*) $St_v = 200$.

3.4. *Streamwise transport of particles inside Qs structures*

This subsection further analyses the mean streamwise momentum flux of particles $\mathcal{F}_M^x$ with respect to the vertical distance from the wall y^+. Figure 10 displays the variation of $\mathcal{F}_M^x$. In the near-wall region, the mean streamwise momentum fluxes inside and outside the Qs structures are nearly the same. However, farther from the wall, the flux outside the Qs structures becomes larger than that inside. This difference can be attributed to the spatial distribution of $Q2$ and $Q4$ structures. As shown in figure 2(*b*), the volume fraction of $Q2$ structures is only slightly greater than that of $Q4$ structures near the wall, but this difference increases significantly at higher positions. According to their definitions, $Q2$ structures are associated with upward-moving fluid that travels slower than the mean streamwise velocity, while $Q4$ structures are associated with downward-moving fluid that travels faster than the mean. Therefore, near the wall, the contribution of $Q4$ structures can nearly balance the momentum flux deficit caused by $Q2$ structures due to their similar volume fractions. As the distance from the wall increases, this compensation becomes insufficient because of the growing disparity between the volume fractions of $Q2$ and $Q4$ structures. It is important to note that although the mean streamwise momentum flux is larger outside the Qs structures, the wall-normal momentum flux is significantly higher within them. This indicates that Qs structures play a particularly efficient role in transporting particles in the wall-normal direction, which is the central focus of this study.

https://doi.org/10.1017/jfm.2025.10284 Published online by Cambridge University Press

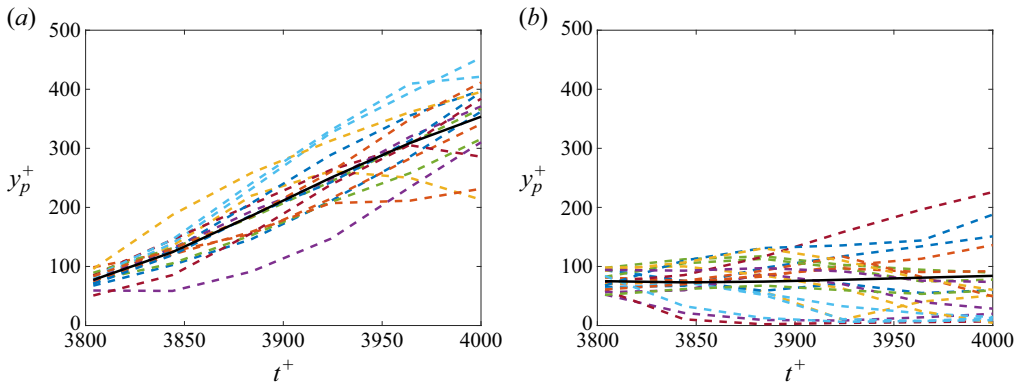


Figure 11. Lagrangian history of the wall-normal position of particles: (*a*) inside Qs structures; (*b*) outside Qs structures. Each coloured dashed line represents the instantaneous wall-normal trajectory of an individual particle, while the black solid line denotes the ensemble-averaged trajectory.

3.5. *Long-distance transport in the wall-normal direction driven by Qs structures*

The results presented in the preceding subsections have demonstrated that both particle number and momentum flux in the wall-normal directions are higher inside the Qs structures compared to outside them, meaning that the wall-normal transport of particles is more efficient inside the Qs structures. While the above analysis focused on the effects of Qs structures on particle transport in an instant, a fundamental question remains: how are inertial particles transported in the wall-normal direction under the continuous influence of the Qs structures?

The Lagrangian history of the wall-normal position of particles is first examined. Previous studies have shown that the lifetime T^+ of typical Qs structures can be approximated by their characteristic height y_{LS}^+, i.e. $T^+ \approx y_{LS}^+$ (Lozano-Durán & Jiménez 2014). This duration is sufficiently long for particles to interact meaningfully with the Qs structures. Although the available data consist of discrete, non-time-resolved snapshots with time interval $\Delta t^+ \approx 40.4$, this resolution is adequate for analysing the Lagrangian trajectories of the wall-normal positions of particles. Particles that remain either inside or outside Qs structures throughout the observation time windows are extracted and analysed, respectively. Figure 11 presents these trajectories, where each coloured dashed line corresponds to the instantaneous wall-normal motion of an individual particle, and the black solid line represents the ensemble-averaged trajectory. It is clear that particles inside the Qs structures undergo larger, directionally wall-normal displacements. In contrast, particles outside the Qs structures exhibit only small vertical displacements or oscillate up and down, resulting in non-directional, wandering motion. This difference is further confirmed by the ensemble-averaged trajectories: particles inside Qs structures move upwards over time, while those outside essentially remain near the same wall-normal level.

To gain deeper insight into the effects of Qs structures on particle transport, the correlations between particle displacement and their interaction frequency with Qs structures are examined. In the channel flow, N_s discrete samples of time snapshots are analysed, capturing both the Qs structures and the particle distribution field. On the one hand, within all sample fields, we track every individual particle, recording its maximum wall-normal height $y_{p,max}$ and its minimum height $y_{p,min}$. The difference $\Delta y_{p,max} = y_{p,max} - y_{p,min}$ represents the largest wall-normal displacement for that particle. l_{max} is

https://doi.org/10.1017/jfm.2025.10284 Published online by Cambridge University Press

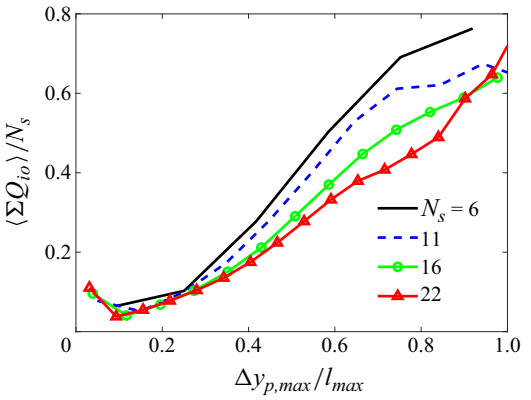


Figure 12. The average occurrence of a particle inside Qs structures, denoted by $\langle \Sigma Q_{io} \rangle$, is plotted against the maximum wall-normal displacement of particles $\Delta y_{p,max}$, in N_s samples. Here, l_{max} is the largest $\Delta y_{p,max}$ among all particles in N_s samples. The particle Stokes number is $St_v = 30$.

the largest displacement $\Delta y_{p,max}$ observed among all sampled particles. On the other hand, a binary variable Q_{io} is defined for each particle, where $Q_{io} = 1$ indicates that the particle is located inside a Qs structure, and $Q_{io} = 0$ indicates the particle is located outside a Qs structure. The quantity $\langle \Sigma Q_{io} \rangle$ then represents the total number of times a given tracked particle is observed inside the Qs structures across all the N_s samples, reflecting its interaction frequency with Qs structures.

Figure 12 shows the correlation between the normalised wall-normal displacement of particles $\Delta y_{p,max}/l_{max}$ and the normalised average occurrence $\langle \Sigma Q_{io} \rangle / N_s$, with particle Stokes number $St_v = 30$ as a representative case. Here, $\langle \Sigma Q_{io} \rangle$ is averaged conditonal on $\Delta y_{p,max}$. Notably, the curves exhibit a monotonic increase when $\Delta y_{p,max}/l_{max} > 0.1$, revealing a distinct positive correlation. This again suggests that particles transported over larger wall-normal displacements tend to reside more frequently inside the Qs structures. Note that the wall-normal transport of a given particle may be influenced by one or multiple Qs structures. In the present analysis, we focus solely on whether the particle resides within Qs structures and is affected by Qs structures, regardless of whether the particle remains inside a single Qs structure or transitions between multiple ones. As the number of samples N_s increases, there is a converging trend in the correlation between the normalised wall-normal displacement of particles and the normalised average occurrence, demonstrating the robustness of the conclusion. In summary, particles can undergo substantial wall-normal displacements under the continuous influence of the Qs structures in wall-bounded turbulence. This can be explained by considering the nature of the Qs structures, which are, by definition, energetically active regions within the flow. When a particle resides inside a Qs structure, it is able to continuously extract energy from the surrounding fluid, enabling sustained transport. As shown in figure 8, such particles tend to maintain relatively high velocities over extended periods. Moreover, Qs structures are characterised by persistent upward or downward motions throughout their long lifetimes (Lozano-Durán & Jiménez 2014), which further facilitates directional particle transport, as illustrated in figure 11. In contrast, particles outside Qs structures experience weaker energy input from the flow, and exhibit more oscillatory, non-directional motion, resulting in significantly shorter transport distances.

https://doi.org/10.1017/jfm.2025.10284 Published online by Cambridge University Press

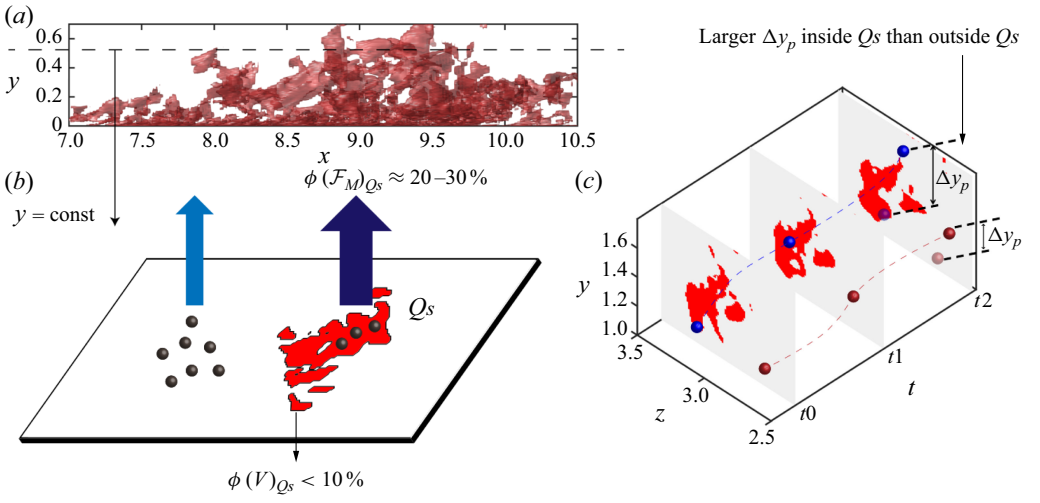


Figure 13. A schematic diagram illustrating the effect of Qs structures on the wall-normal transport of particles in turbulent channel flow. (*a*) Side view of instantaneous Qs structures extracted from the flow field. (*b*) Illustration of a wall-parallel plane. The red patches represent Qs structures, and the spheres indicate particles located either inside or outside Qs structures. The number of spheres reflects the approximate proportion of particles inside and outside Qs structures. Blue arrows indicate wall-normal particle momentum fluxes, with the light blue arrow representing fluxes outside Qs structures, and the dark blue arrow representing fluxes inside. The wider dark blue arrow indicates that Qs structures, though occupying a small fraction of the total volume ($\phi(V)_{Qs} < 10\,\%$), contribute a disproportionately large share of the total particle momentum flux [$\phi(\mathcal{F}_M)_{Qs} \approx 20{-}30\,\%$]. (*c*) Illustration of particle trajectories relative to Qs structures. Red patches denote Qs structures, while blue spheres represent particles transported inside Qs structures, and red spheres represent particles transported outside. Dashed lines trace the particle trajectories across three instants ($t0$, $t1$ and $t2$), with spheres shown at each time step. To better illustrate the wall-normal displacement, the initial position at time $t0$ is also marked at time $t2$, and the vertical distance between the two is annotated as Δy_p, indicating the wall-normal displacement of the particle. This schematic demonstrates that particles inside Qs structures tend to travel longer vertical distances, emphasising their key role in enhancing wall-normal transport.

4. Conclusions

The effect of Qs structures on the wall-normal transport of particles in turbulent channel flow at $Re_\tau = 1000$ has been analysed by data from direct numerical simulations. The particle flux and transport efficiency are quantified in the presence of the Qs structures.

A schematic diagram (figure 13) is drawn to illustrate the effects of Qs structures on the particle transport. Despite occupying a small volume fraction of the domain, Qs structures play a crucial role in the wall-normal transport of both fluid momentum and particles. Both particle number and momentum flux inside the Qs structures are larger than those outside them. Additionally, the fraction of wall-normal momentum flux inside Qs structures exceeds the volume fraction of Qs structures, indicating an enhanced transport efficiency inside the Qs structures. The effectiveness of Qs structures in transporting inertial particles becomes more pronounced as particle inertia decreases. Furthermore, the continuous effect of Qs structures on particles is explored. As shown in figure 13(*c*), particles are transported to larger wall-normal locations under the continuous influence of the Qs structures compared to the particles outside. This implies that the transport of particles, such as sand particles during a storm, could potentially be estimated by identifying Qs structures in turbulent flows, as revealed by our findings.

https://doi.org/10.1017/jfm.2025.10284 Published online by Cambridge University Press

Funding. This work is supported by the Natural Science Foundation of China (grant nos 12388101, 92252104 and 92252204).

Declaration of interests. The authors report no conflict of interest.

References

Baker, L., Frankel, A., Mani, A. & Coletti, F. 2017 Coherent clusters of inertial particles in homogeneous turbulence. *J. Fluid Mech.* **833**, 364–398.

Berk, T. & Coletti, F. 2020 Transport of inertial particles in high-Reynolds-number turbulent boundary layers. *J. Fluid Mech.* **903**, A18.

Bernardini, M. 2014 Reynolds number scaling of inertial particle statistics in turbulent channel flows. *J. Fluid Mech.* **758**, R1.

Bernardini, M., Pirozzoli, S. & Orlandi, P. 2013 The effect of large-scale turbulent structures on particle dispersion in wall-bounded flows. *Intl J. Multiphase Flow* **51**, 55–64.

Bo, T.L. 2021 The effect of turbulent motions on the transport of dust and heat in the development stage of dust storms induced by cold front. *J. Wind Engng Indust. Aerodyn.* **212**, 104604.

Bragg, A.D., Richter, D.H. & Wang, G. 2021 Settling strongly modifies particle concentrations in wall-bounded turbulent flows even when the settling parameter is asymptotically small. *Phys. Rev. Fluids* **6** (12), 124301.

Caporaloni, M., Tampieri, F., Trombetti, F. & Vittori, O. 1975 Transfer of particles in nonisotropic air turbulence. *J. Atmos. Sci.* **32** (3), 565–568.

Costa, P., Brandt, L. & Picano, F. 2020 Interface-resolved simulations of small inertial particles in turbulent channel flow. *J. Fluid Mech.* **883**, A54.

Eaton, J.K. & Fessler, J.R. 1994 Preferential concentration of particles by turbulence. *Intl J. Multiphase Flow* **20**, 169–209.

Fessler, J.R., Kulick, J.D. & Eaton, J.K. 1994 Preferential concentration of heavy particles in a turbulent channel flow. *Phys. Fluids* **6** (11), 3742–3749.

Gao, W., Samtaney, R. & Richter, D. 2023 Direct numerical simulation of particle-laden flow in an open channel at $Re_\tau = 5186$. *J. Fluid Mech.* **957**, A3.

Haller, G. 2015 Lagrangian coherent structures. *Annu. Rev. Fluid Mech.* **47** (1), 137–162.

Jie, Y., Andersson, H.I. & Zhao, L. 2021 Effects of the quiescent core in turbulent channel flow on transport and clustering of inertial particles. *Intl J. Multiphase Flow* **140**, 103627.

Jie, Y., Cui, Z., Xu, C. & Zhao, L. 2022 On the existence and formation of multi-scale particle streaks in turbulent channel flows. *J. Fluid Mech.* **935**, A18.

Jiménez, J. 2018 Coherent structures in wall-bounded turbulence. *J. Fluid Mech.* **842**, P1.

Liu, L., Li, X., Tian, X., Zhang, X., Xu, L. & Zhang, X. 2023 Numerical investigation on inclined hydraulic transport of large particles for deepsea mining. *China Ocean Engng* **37** (3), 420–432.

Liu, Y., Shen, L., Zamansky, R. & Coletti, F. 2020 Life and death of inertial particle clusters in turbulence. *J. Fluid Mech.* **902**, R1.

Lozano-Durán, A., Flores, O. & Jiménez, J. 2012 The three-dimensional structure of momentum transfer in turbulent channels. *J. Fluid Mech.* **694**, 100–130.

Lozano-Durán, A. & Jiménez, J. 2014 Time-resolved evolution of coherent structures in turbulent channels: characterization of eddies and cascades. *J. Fluid Mech.* **759**, 432–471.

Lu, H., Wang, B., Zhang, H. & Wang, X. 2013 Transports of air particulate matters in the atmospheric boundary layer – numerical studies using Eulerian and Lagrangian methods. *Sci. China Phys. Mech. Astron.* **56** (3), 645–650.

Lu, S.S. & Willmarth, W.W. 1973 Measurements of the structure of the Reynolds stress in a turbulent boundary layer. *J. Fluid Mech.* **60** (3), 481–511.

Marchioli, C. & Soldati, A. 2002 Mechanisms for particle transfer and segregation in a turbulent boundary layer. *J. Fluid Mech.* **468**, 283–315.

Marusic, I., Mathis, R. & Hutchins, N. 2010 High Reynolds number effects in wall turbulence. *Intl J. Heat Fluid Flow* **31** (3), 418–428.

Milici, B., Marchis, M.D., Sardina, G. & Napoli, E. 2014 Effects of roughness on particle dynamics in turbulent channel flows: a DNS analysis. *J. Fluid Mech.* **739**, 465–478.

Monchaux, R., Bourgoin, M. & Cartellier, A. 2010 Preferential concentration of heavy particles: a Voronoï analysis. *Phys. Fluids* **22** (10), 103304.

Motoori, Y., Wong, C. & Goto, S. 2022 Role of the hierarchy of coherent structures in the transport of heavy small particles in turbulent channel flow. *J. Fluid Mech.* **942**, A3.

https://doi.org/10.1017/jfm.2025.10284 Published online by Cambridge University Press

NILSEN, C., ANDERSSON, H.I. & ZHAO, L. 2013 A Voronoï analysis of preferential concentration in a vertical channel flow. *Phys. Fluids* **25** (11), 115108.
PICANO, F., SARDINA, G. & CASCIOLA, C.M. 2009 Spatial development of particle-laden turbulent pipe flow. *Phys. Fluids* **21** (9), 093305.
REEKS, M.W. 1983 The transport of discrete particles in inhomogeneous turbulence. *J. Aerosol Sci.* **14** (6), 729–739.
SARDINA, G., PICANO, F., SCHLATTER, P., BRANDT, L. & CASCIOLA, C.M. 2011 Large scale accumulation patterns of inertial particles in wall-bounded turbulent flow. *Flow Turbul. Combust.* **86** (3), 519–532.
SARDINA, G., SCHLATTER, P., BRANDT, L., PICANO, F. & CASCIOLA, C.M. 2012 Wall accumulation and spatial localization in particle-laden wall flows. *J. Fluid Mech.* **699**, 50–78.
SCHERER, M., UHLMANN, M., KIDANEMARIAM, A.G. & KRAYER, M. 2022 On the role of turbulent large-scale streaks in generating sediment ridges. *J. Fluid Mech.* **930**, A11.
SCHILLER, L. & NAUMANN, A.Z. 1933 Ueber die grundlegenden Berechnungen bei der Schwerkraftaufbereitung. *Ver. Deut. Ing.* **77**, 318–320.
SOLDATI, A. & MARCHIOLI, C. 2009 Physics and modelling of turbulent particle deposition and entrainment: review of a systematic study. *Intl J. Multiphase Flow* **35** (9), 827–839.
WALLACE, J.M., ECKELMANN, H. & BRODKEY, R.S. 1972 The wall region in turbulent shear flow. *J. Fluid Mech.* **54** (1), 39–48.
WANG, G. & RICHTER, D. 2020 Multiscale interaction of inertial particles with turbulent motions in open channel flow. *Phys. Rev. Fluids* **5** (4), 044307.
WEI, Q., WANG, P. & ZHENG, X. 2024 Modulations of turbulent/non-turbulent interfaces by particles in turbulent boundary layers. *J. Fluid Mech.* **983**, A15.
WILLMARTH, W.W. & LU, S.S. 1972 Structure of the Reynolds stress near the wall. *J. Fluid Mech.* **55** (1), 65–92.
XIAO, S., CUI, Y., BRAHNEY, J., MAHOWALD, N.M. & LI, Q. 2023 Long-distance atmospheric transport of microplastic fibres influenced by their shapes. *Nat. Geosci.* **16** (10), 863–870.
YUAN, W., ZHAO, L., ANDERSSON, H.I. & DENG, J. 2018 Three-dimensional Voronoï analysis of preferential concentration of spheroidal particles in wall turbulence. *Phys. Fluids* **30** (6), 063304.
ZHAO, L. & ANDERSSON, H.I. 2012 Statistics of particle suspensions in turbulent channel flow. *Commun. Comput. Phys.* **11** (4), 1311–1322.

https://doi.org/10.1017/jfm.2025.10284 Published online by Cambridge University Press